RESEARCH ARTICLE

Hierarchical porous carbon derived from one-step self-activation of zinc gluconate for symmetric supercapacitors with high energy density

Junlei Xiao[1], **Hua Zhang** (✉)[2], **Yifan Wang**[1], **Chunmei Zhang** (✉)[3], **Shuijian He**[1], **Shaohua Jiang** (✉)[1]

1 Jiangsu Co-Innovation Center of Efficient Processing and Utilization of Forest Resources, International Innovation Center for Forest Chemicals and Materials, College of Materials Science and Engineering, Nanjing Forestry University, Nanjing 210037, China
2 College of Chemistry and Chemical Engineering, Jiangxi Normal University, Nanchang 330022, China
3 Institute of Materials Science and Devices, School of Materials Science and Engineering, Suzhou University of Science and Technology, Suzhou 215009, China

Abstract   Porous carbons with high specific area surfaces are promising electrode materials for supercapacitors. However, their production usually involves complex, time-consuming, and corrosive processes. Hence, a straightforward and effective strategy is presented for producing highly porous carbons via a self-activation procedure utilizing zinc gluconate as the precursor. The volatile nature of zinc at high temperatures gives the carbons a large specific surface area and an abundance of mesopores, which avoids the use of additional activators and templates. Consequently, the obtained porous carbon electrode delivers a satisfactory specific capacitance and outstanding cycling durability of 90.9% after 50000 cycles at 10 A·g^{-1}. The symmetric supercapacitors assembled by the optimal electrodes exhibit an acceptable rate capability and a distinguished cycling stability in both aqueous and ionic liquid electrolytes. Accordingly, capacitance retention rates of 77.8% and 85.7% are achieved after 50000 cycles in aqueous alkaline electrolyte and 10000 cycles in ionic liquid electrolyte. Moreover, the symmetric supercapacitors deliver high energy/power densities of 49.8 W·h·kg^{-1}/2477.8 W·kg^{-1} in the Et$_4$NBF$_4$ electrolyte, outperforming the majority of previously reported porous carbon-based symmetric supercapacitors in ionic liquid electrolytes.

Keywords   self-activation, zinc organic salts, abundant mesopores, symmetric supercapacitor, liquid electrolyte

1   Introduction

The rapid development of compact and portable energy storage devices triggers a pressing need for power sources that are able to achieve high energy density and power density [1–5]. In this regard, supercapacitors have emerged as promising power supplies due to their high power density, rapid charge–discharge rate, and distinguished cycling durability [6–8]. Unfortunately, the practical applications of supercapacitors have been hampered seriously by their low energy densities, which need significant improvement [9–12]. As the core component of a supercapacitor, the electrode material substantially determines the overall performance of supercapacitors. Among various electrode materials, carbon materials with high porosity and conductivity are widely adopted as the electrode material for supercapacitors owing to their low-cost, abundant raw materials, large specific area, and outstanding chemical stability [13–18]. Particularly, activated carbons have already been used in commercial capacitors, which allow a rapid charge–discharge rate and outstanding cyclability [19,20]. However, the activated carbon-based supercapacitors usually suffer from low energy density (ca. < 10 W·h·kg^{-1}) due to their dominant micropores structure [15,21]. Although such pore structures provide adequate room for ion adsorption, they further provide an unfavorable specific capacitance and inferior rate capability because of their large diffusion channel and substantial ion diffusion resistance [22–25]. Therefore, the development of hierarchical porous carbons with controlled porosity, high specific surface area, and interconnected pore structure is substantially desired. Furthermore, difficult synthesis procedures (such

as carbonatization and activation), potent corrosives, and subpar ion-transport kinetics affect the production of activated carbons [6,16,18,26].

In general, hierarchical porous carbons are fabricated through a two-step approach including the pyrolysis of organic precursor accompanied by a hard/soft template, followed by a chemical activation [27,28]. Abundant activation agents have been used for chemical activation, such as metal hydroxides and carbonates/bicarbonates (e.g., KOH, K_2CO_3, $KHCO_3$, and $NaHCO_3$), and metal chlorides (e.g., $ZnCl_2$ and $CaCl_2$) [29]. Among them, KOH activation is the most powerful and widely used approach. Nevertheless, it suffers from strong corrosive effects and high consumption, hampering its application for industrial production [30,31]. Moreover, although it is not as effective as KOH activation, zinc salt activation, such as $ZnCl_2$, significantly extends the pore textures of porous carbon. However, the $ZnCl_2$ activation is also corrosive and results in severe contamination. Recently, due to the intrinsic microstructure of biomass-based precursors, the synthesis of porous carbons generated from such materials is exceedingly attractive, substantially simplifying the synthetic process [20,32,33]. However, it is challenging to modify the pore structure of carbon generated from biomass [34,35]. Therefore, while it is appealing, creating a simple and effective method to prepare extremely porous carbons is still a difficult task [13,36].

Herein, a straightforward and effective procedure for creating hierarchical porous carbons is reported, utilizing zinc gluconate as the precursor without adding any activators or templates. This approach only requires one-step carbonization of organic zinc salt precursors, without any additional post-activation steps. Compared to KOH and $ZnCl_2$ activations, the use of organic zinc gluconate presents far less corrosion to facilities and simultaneously serves as the carbon source, template, and activation agent. The organic matrix and its derived carbon matrix will limit the growth of inorganic intermediate products, giving rise to the production of highly micro-/mesoporous pore structures. The pyrolysis of zinc gluconate is analogous to the carbonization of Zn-containing metal–organic frameworks (MOFs), in which the organic ligands are converted into carbon and the non-corrosive Zn evaporates out at a high temperature, thus realizing a self-activation process. Notably, the precursors that are used in this study are less expensive and more readily accessible than Zn-containing MOFs, providing an affordable and viable method for the mass manufacturing of extremely porous carbons. As a result, the porous carbons made from zinc gluconate (ZnPCs) possess a hierarchical porous structure and a great deal of mesopores and micropores, which results in a high specific capacitance, outstanding rate performance, and improved cycle stability. Furthermore, the ZnPCs-based symmetric supercapacitors exhibit distinguished energy density and prolonged cycle durability in the ionic liquid electrolyte, outperforming the majority of previous works.

2 Experimental

2.1 Preparation and characterization of ZnPCs

First, 1.0 g of commercial zinc gluconate ($C_{12}H_{22}O_{14}Zn$, ⩾ 99.9%) was placed in a corundum crucible and annealed at 750–1050 °C for 2 h under an N_2 atmosphere with a heating rate of 8 °C·min^{-1}. Subsequently, the products were soaked in a 1.0 mol·L^{-1} aqueous hydrochloric acid solution for 24 h and washed afterwards with deionized water until the pH value became neutral. Finally, the resultant products were dried at 60 °C in an oven. For convenience, the obtained porous carbons derived from zinc gluconate were denoted as ZnPC-T, where T stands for carbonized temperatures (T = 750, 850, 950, and 1050 °C). The carbon yields of ZnPC-750, ZnPC-850, ZnPC-950, and ZnPC-1050 were 15.5, 13.9, 10.3, and 8.2 wt %, respectively.

Transmission electron microscopy (TEM, JEM-2010) at 200 kV and scanning electron microscopy (SEM, JEOL JSM-6480) at 5 kV were used to analyze the morphology and microstructure of ZnPCs. The crystalline structure of the obtained samples was analyzed using X-ray diffraction (XRD, SmartLab3K) and Raman spectroscopy (XPLORA PLUS). Raman spectra were recorded using a laser at an excitation wavelength of 532 nm. The porous structure of the ZnPCs was measured by nitrogen adsorption/desorption isotherms at 77 K with a Micromeritics apparatus (ASAP 2020). Moreover, the Brunauer–Emmett–Teller method was used to calculate the specific surface area, while the Barrett–Joyner–Halenda method was used to analyze the pore size distribution of the ZnPCs. Thermogravimetric analysis (TGA) was employed to study the thermal decomposition behaviors of the ZnPC sample under the protection of N_2 gas with a ramping rate of 8 °C·min^{-1}.

2.2 Electrochemical measurements

All electrochemical performances incorporating cyclic voltammogram (CV), galvanostatic charge/discharge (GCD), and electrochemical impendence spectroscopy (EIS) were performed and recorded on an electrochemical working station (CHI760E, Chenhua, Shanghai, China). In this setting, for the working electrode preparation, the as-prepared ZnPCs, acetylene black, and polyvinylidene difluoride were mixed in N-methylpyrrolidone to form active material slurry with a mass ratio of 8:1:1. The obtained slurry was subsequently coated with nickel foam (1 cm × 1 cm × 0.1 cm) and then dried at 60 °C for 12 h

under a vacuum. For the three-electrode system, the electrochemical performance was tested in a 6 mol·L^{-1} KOH electrolyte using nickel foam loaded with ZnPC samples as the working electrode, an Hg/HgO electrode as the reference electrode, and Pt foil as the counter electrode. As for the two-electrode system, a symmetric supercapacitor was constructed using ZnPC-950 as both positive and negative electrodes, and thereafter tested in 6 mol·L^{-1} KOH or tetraethylammonium tetrafluoroborate (Et$_4$NBF$_4$) electrolyte. The mass loading of ZnPCs in each working electrode was about 2 mg.

For the three-electrode test, the specific capacitance C (F·g^{-1}) was calculated from GCD curves:

$$C = \frac{I\Delta t}{m\Delta V}, \tag{1}$$

where I (A) and Δt (s) are respectively the discharge current and time, ΔV (V) is the potential window, and m (g) is the total mass of the active material of the working electrode. Referring to the two-electrode test, the capacitances of the supercapacitor were calculated as:

$$C_t = \frac{2I\Delta t}{m\Delta V}, \tag{2}$$

where C_t (F·g^{-1}) is the total capacitance of the device and m (g) is the single mass of two electrodes. The specific energy density (E, W·h·kg^{-1}) and specific power density (P, W·kg^{-1}) of the symmetrical supercapacitor device were calculated using Eqs. (3) and (4), respectively:

$$E = \frac{1}{2}C_t\Delta V^2, \tag{3}$$

$$P = \frac{E}{\Delta t}. \tag{4}$$

3   Results and discussion

3.1   Characterization of the ZnPCs

Figure 1 and Fig. S1 (cf. Electronic Supplementary Material, ESM) demonstrate the surface morphology and porous structure of as-prepared ZnPCs. Commonly available organic zinc gluconate was employed directly as precursor materials and pyrolyzed at high temperatures to produce the porous carbons (Fig. 1(a)). The organic compounds in the precursors were converted to carbon during the pyrolysis process, and the produced Zn species (e.g., zinc oxides) were reduced to Zn(0). Zn evaporated off after the pyrolysis temperature reached the boiling point (907 °C), and the Zn vapor flowed through the carbon matrix and created multiple voids, resulting in highly porous carbons with a significant amount of specific surface area. The pyrolysis of zinc gluconate was investigated using TGA (Fig. 1(b)). The first weight loss ending at ~160 °C is mainly attributed to the combined water in zinc gluconate. The second stage ranging from ~200 to ~550 °C is ascribed to the thermal degradation of glycosidic bonds. After 550 °C, the organic compound started to convert into the carbon matrix and Zn gradually sublimed with the pyrolysis temperature increase, resulting in the porous structure formed on the surface of the ZnPCs [32,37,38]. Simultaneously, the partial zinc oxide generated during pyrolysis underwent a metallo-thermic reduction reaction with carbon, further reducing the yield of the resultant carbon products. The pyrolysis of zinc gluconate yielded irregular vesiculated particles with a two-dimensional sheet structure. As expected, the pyrolysis temperature had a significant impact on the
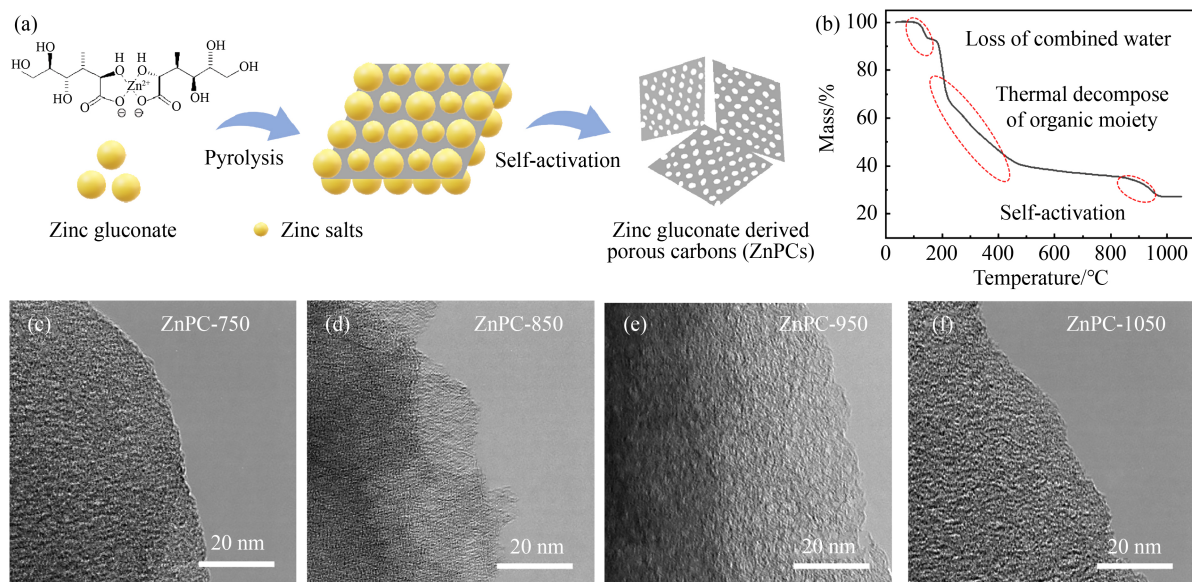

Fig. 1 Synthesis and characterization of the ZnPCs: (a) Schematic illustration of the preparation of porous carbons (ZnPCs) using zinc gluconate as the precursor; (b) TGA curve of zinc gluconate; (c–f) TEM images of the ZnPCs.

porosity structure of the ZnPCs. At low temperatures of 750 and 850 °C, no noticeable holes were visible on the surface of the ZnPCs (Figs. 1(c, d) and Figs. S1(a, b)). When the pyrolysis temperature reached 950 °C, the sheet structures largely disintegrated into tiny particles and a significant number of mesopores and micropores on the carbon skeleton have developed due to zinc evaporation (Fig. 1(e) and Fig. S1(c)). As the temperature rose higher, a bulk structure forms that may be attributed to the substantial collapse of pore structures and were then sintered into a single piece at 1050 °C (Fig. 1(f) and Fig. S1(d)). These results indicate that an appropriate carbonization temperature (e.g., 950 °C) is beneficial to forming a 3D interconnected porous structure, which is advantageous for the storage and transportation of electrolyte ions.

XRD and Raman measurements were further performed to character the crystalline structure of the ZnPCs (Fig. 2). As shown in Fig. 2(a), two broad diffraction peaks at around 23° and 44°, corresponding to the reflections of the (002) and (101) crystal planes of graphite, were

visible in the XRD patterns of all ZnPC samples. The broad bump at 23° revealed the amorphous character of the obtained carbon samples. Two distinct peaks at ~1340 cm^{-1} (D-band) and ~1580 cm^{-1} (G-band) were observed in Raman spectra (Fig. 2(b)), which are associated with graphitic sp2 carbon structures and defects, respectively. The degree of graphitization and flaws in carbon materials is shown by the relative intensity ratio of the D and G bands (I_D/I_G). The I_D/I_G value of as-prepared ZnPCs progressively rose to 1.66 as the pyrolysis temperature rose from 750 to 950 °C (Fig. 2(b) and Table 1), illustrating the rise in the degree of disorder and flaws of the carbon materials brought on by the production of porous structures. At 1050 °C, this I_D/I_G value decreased to 1.55 due to the increase in the degree of graphitization of the carbon material. Both the strong D bands and high I_D/I_G values demonstrate that all the ZnPC samples are amorphous carbon structures with a variety of defects and disorders. All of the N_2 adsorption–desorption isotherms of ZnPC samples exhibit a characteristic I adsorption type (Fig. 2(c)), which is
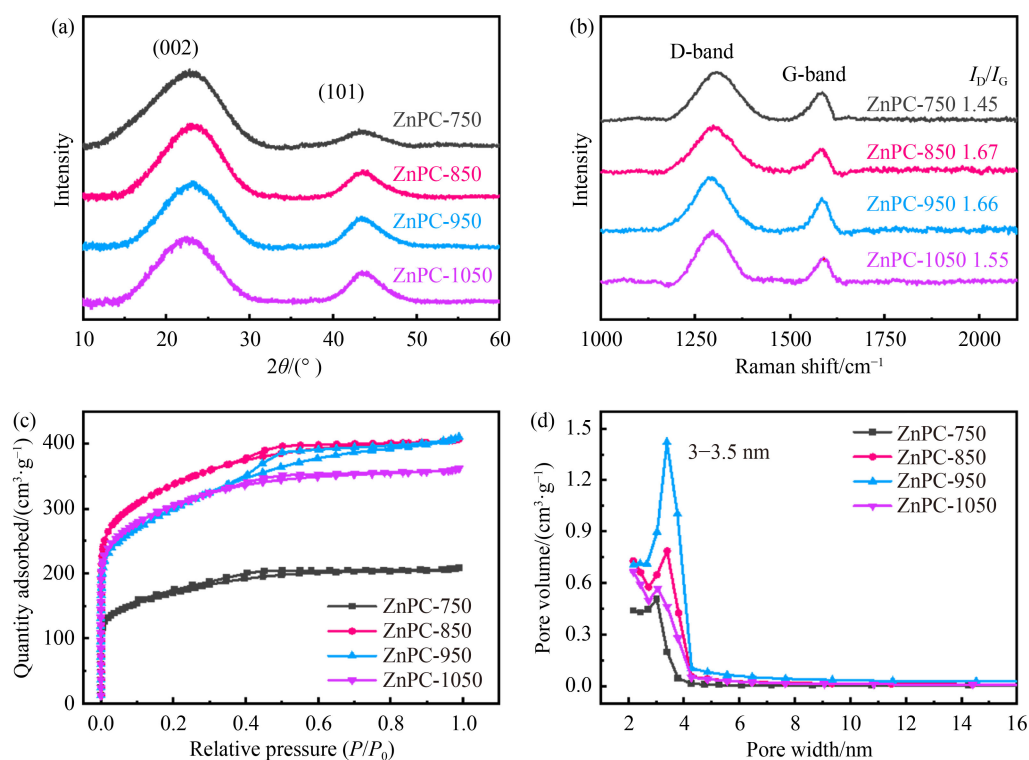

Fig. 2 Physical properties of the ZnPCs samples: (a) XRD patterns, (b) Raman spectra, (c) N$_2$ adsorption−desorption isotherms, and (d) pore sizes distribution of ZnPC-750, ZnPC-850, ZnPC-950, and ZnPC-1050, respectively.

Table 1 Pore structure parameters of the ZnPC samples

Sample	S_{BET}/(m$^2 \cdot$g^{-1})	V_{total}/(cm$^3 \cdot$g^{-1})	V_{micro}/(cm$^3 \cdot$g^{-1})	V_{meso}/(cm$^3 \cdot$g^{-1})	I_D/I_G
ZnPC-750	608.84	0.32	0.12	0.20	1.45
ZnPC-850	1226.64	0.63	0.27	0.36	1.67
ZnPC-950	1071.63	0.64	0.19	0.45	1.66
ZnPC-1050	1108.49	0.56	0.25	0.31	1.55

characterized by significant nitrogen adsorption at low relative pressures and a clear H4 hysteresis loop in the region of $P/P_0 > 0.4$. These findings are compatible with the TEM results and confirm the presence of hierarchical porous structure. As shown in Table 1, with the pyrolysis temperature, both the specific surface area and the total pore volume increase first and then decrease. The aforementioned decrease at higher temperatures of 950 and 1000 °C could be attributed to the collapse of fragile pore structures. As a result, the ZnPC-950 exhibits the highest pore volume of 0.64 $cm^3 \cdot g^{-1}$ and the specific surface area of 1072 $m^2 \cdot g^{-1}$, which is expected to improve the capacitance and rate performance. Furthermore, the pore size distribution of all ZnPCs samples is extremely similar; mainly centered at about 3.0–3.5 nm (Fig. 2(d)).

3.2 Electrochemical performance of ZnPC samples

The supercapacitor capabilities of the ZnPCs were initially evaluated in a traditional three-electrode system and the corresponding results are presented in Fig. 3 and Figs. S(2–4) (cf. ESM). The CV curves of all ZnPC samples in Fig. 3(a) have a reasonable rectangular shape, proving that the electrical double-layer capacitance (EDLC) is primarily responsible for the specific capacitance. The superior specific capacitance of ZnPC-950 is indicated by its larger integral area. Simultaneously, compared with other ZnPC electrodes, the ZnPC-950 shows the highest mass-specific capacitance at all current

densities (Fig. 3(b)). Hence, it is worth noting that although the ZnPC-850 has a larger specific surface area, its specific capacitance is inferior to that of the ZnPC-950. The reason can be explained as follows. Generally, a micropores (< 2 nm) structure is able to provide an efficient electrode−electrolyte interface area for the formation of an electric double-layer capacitor, while the ion infiltration into these micropores is challenging, resulting in relatively low kinetics. Lager macropores (> 50 nm) and mesopores (2–50 nm), on the other hand, are capable of acting as ion-buffering reservoirs and transportation pathways to access the micropores [39]. In this context, macropores serve as electrolyte reservoirs for reducing the ion diffusion distance [40]. The largest specific capacitance of the ZnPC-950 can be attributed to its larger mesopores and similar micropores volume than the ZnPC-850, leading to fast ion transportation to access the micropore, thus providing a superior specific capacitance. To further shed insights on the resistive and capacitive behavior of the ZnPC samples, electrochemical impedance spectroscopy measurements were performed. As shown in Fig. 3(c), the obtained Nyquist plots of all ZnPC samples are composed of a semicircle in the high-frequency and a straight line in the low-frequency. The equivalent circuit model (inset in Fig. 3(c), down panel) consists of the solution resistance (R_s), the charge transfer resistance (R_{ct}), and the Warburg impedance (Z_w). The CPE_{dl} is the constant phase element that represents double layer capacitance at interfaces between solids and ionic solutions owing to ionic and/or electronic charge
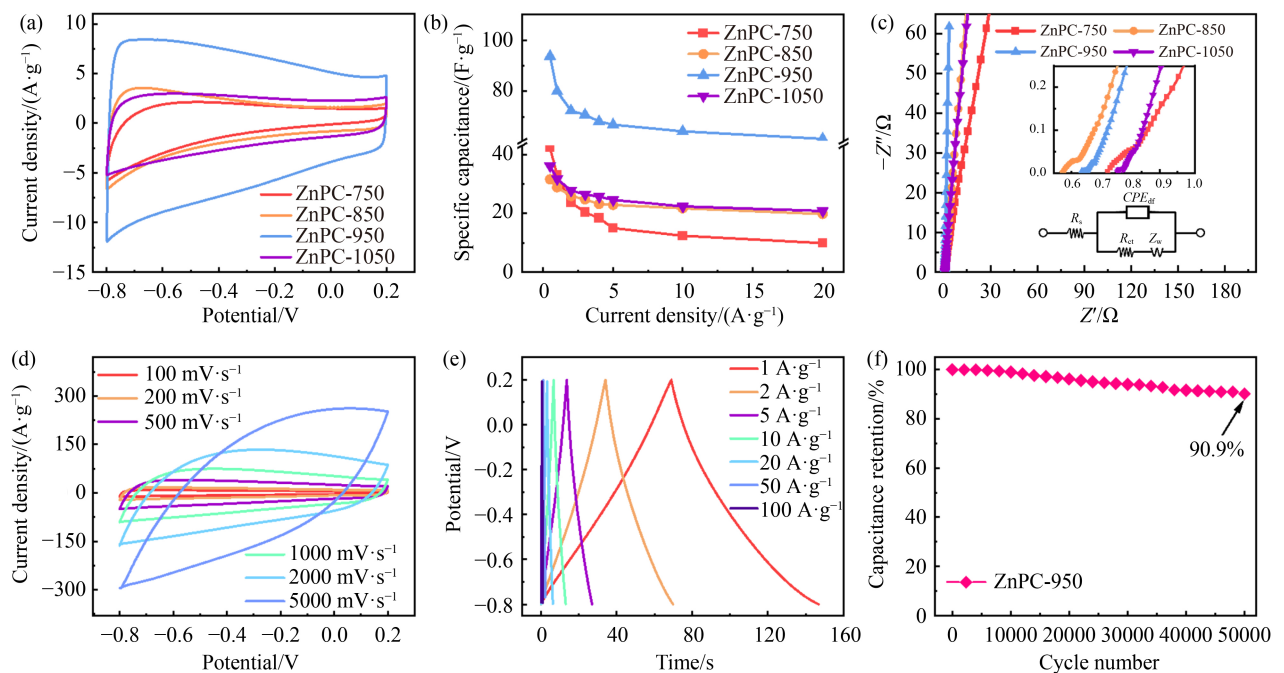

Fig. 3 Electrochemical performance of as-prepared ZnPCs in a 6 mol·L^{-1} KOH solution: (a) CV curves at 100 mV·s^{-1}, (b) specific capacitance of ZnPCs at various current densities, (c) Nyquist plots of the ZnPCs (The inset in (c) is the corresponding enlarged picture and the equivalent circuit diagram), (d) CV curves of the ZnPC-950 electrode at various scan rates, (e) GCD curves of the ZnPC-950 at multiple current densities, and (f) cycling stability of the ZnPC-950 electrode at 10 A·g^{-1}.

separation. Table S1 (cf. ESM) compares the corresponding fitting parameters of ZnPC samples. Consequently, the R_s and R_{ct} values of the ZnPC-950 are 0.68 and 0.045 Ω, respectively. Compared with other samples, the ZnPC-950 shows the lowest R_{ct} due to its large mesopores and micropores, which facilitate the diffusion of the ions and thus improve the capacitance and rate capability. Therefore, the ZnPC-950 is the optimal electrode and it is used for further measurements. As shown in Fig. 3(d), all of the CV curves of the ZnPC-950 electrode show a rectangular-like shape. Even at a high scan rate of 200 mV·s^{-1}, this rectangular shape retains well, demonstrating an exceptional rate capability. Likewise, the GCD curves of the ZnPC-950 electrode present a symmetrical triangle (Fig. 3(e)), suggesting good charge–discharge characteristics. The long-term cycling performance of the ZnPC-950 electrode was further evaluated at a high current density of 10 A·g^{-1}. Impressively, the capacitance retention rate of the ZnPC-950 electrode reached 90.9% (Fig. 3(f)), indicating its outstanding cycling stability.

To further explore the practical application, a symmetric supercapacitor consisting of two identical ZnPC-950 electrodes was assembled and subsequently tested in an aqueous alkaline solution and an Et$_4$NBF$_4$ ionic liquid electrolyte (Figs. 4 and S(5–6), cf. ESM), respectively. The quasi-rectangular CV curves at various scan rates in Fig. 4(a) reveal the dominant EDLC behavior of the ZnPC-950//ZnPC-950 symmetric supercapacitor. Furthermore, the nearly symmetric GCD curves maintained a nearly ideal EDLC behavior and a

satisfactory power property with a low voltage drop of 0.15 V at 1.0 A·g^{-1} (Fig. 4(b)). The symmetric supercapacitor was able to deliver a specific capacitance of 66 F·g^{-1} at 1 A·g^{-1}, which still maintained 77.9% at 10 A·g^{-1} and 50.5% at 20 A·g^{-1} (Fig. S5(a), cf. ESM), respectively. Even at a high current density of 10 A·g^{-1}, adequate capacitance retention of 77.8% was achieved after 50000 cycles (Fig. 4(c)). Moreover, the Nyquist impedance plots of the ZnPC-950//ZnPC-950 symmetric supercapacitor showed a nearly vertical EIS curve and a low charge-transfer resistance (Fig. S5(b), cf. ESM). As a result, the ZnPC-950//ZnPC-950 symmetric supercapacitor delivered an energy density of 8.8 W·h·kg^{-1} at the power density of 976.8 W·kg^{-1} in a 6 mol·L^{-1} KOH electrolyte.

In this setting, an ionic liquid electrolyte (Et$_4$NBF$_4$) was introduced to replace the alkaline electrolyte to further improve the energy density and power density of the devices, which could increase the voltage window of the symmetric supercapacitor. As a result, the ZnPC-950//ZnPC-950 symmetric supercapacitor in the Et$_4$NBF$_4$ electrolyte operated at a large voltage window of 0–2.5 V (Fig. 4(d)), which was significantly wider than that in the 6 mol·L^{-1} KOH electrolyte. Simultaneously, both the quasi-rectangular CV curves and nearly symmetric GCD curves (Fig. S6(a), cf. ESM) in Et$_4$NBF$_4$ electrolytes indicate good EDLC behavior. Furthermore, the ZnPC-950//ZnPC-950 symmetric supercapacitor in the Et$_4$NBF$_4$ electrolyte exhibited a minor internal resistance and a low transfer resistance (Fig. S6(b), cf. ESM). After 10000 charge–discharge cycles at 10 A·g^{-1}, the capacitance
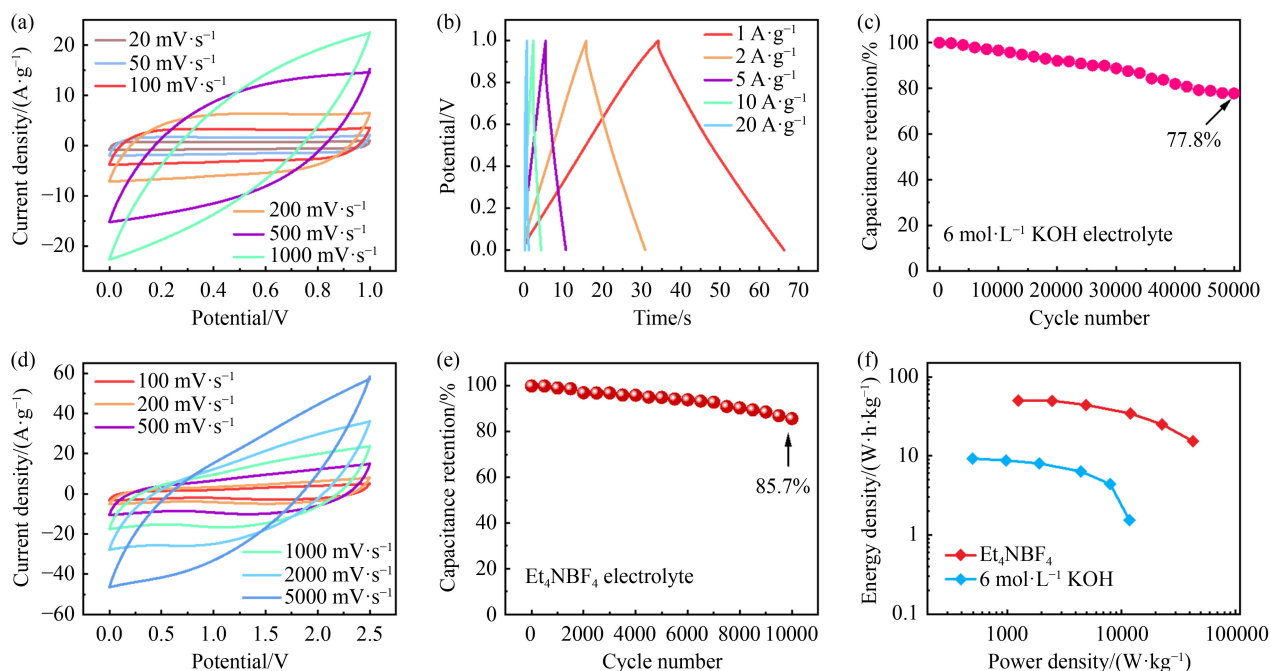

Fig. 4 Electrochemical performance of the symmetric supercapacitor based on ZnPC-950 electrodes: (a) CV curves and (b) GCD curves of the symmetric supercapacitor in a 6 mol·L^{-1} KOH electrolyte; (c) cycling stability of the symmetric supercapacitor in a 6 mol·L^{-1} KOH electrolyte at a current density of 10 A·g^{-1}; (d) CV curves and (e) cycling stability of the symmetric supercapacitor in an Et$_4$NBF$_4$ electrolyte; (f) Ragone plots of the symmetric supercapacitor in a 6 mol·L^{-1} KOH and Et$_4$NBF$_4$ electrolytes.

retention reached 85.7% (Fig. 4(e)), demonstrating adequate cycling stability in ionic liquid electrolytes. Figure 4(f) displays the Ragone plots of ZnPC-950//ZnPC-950 symmetric supercapacitor in different electrolytes. Moreover, the maximum gravimetric energy density in Et_4NBF_4 electrolyte was as high as 49.8 $W·h·kg^{-1}$ at the power density of 2477.8 $W·kg^{-1}$ (Fig. 4(f)), which is about six times higher than that in a 6 $mol·L^{-1}$ KOH electrolyte. Notably, the energy density of ZnPC-950//ZnPC-950 symmetric supercapacitor in Et_4NBF_4 electrolyte outperforms the majority of the previously reported porous carbon-based symmetric supercapacitors in ionic liquid electrolytes [41–44]. This outstanding performance is attributed to the abundant micropores and narrow mesopores on the carbon skeletons, which are beneficial for storing up enough electrolytes in ionic liquid.

4   Conclusions

In summary, a facile and effective self-activation process to prepare highly porous carbons with abundant pore structures through direct pyrolysis of zinc gluconate is demonstrated. Compared with the conventional two-step procedure, the suggested process is more convenient and avoids the use of activators and templates due to the volatile character of zinc. The obtained ZnPCs possess a high specific surface area and abundant mesopores and micropores, which are beneficial for storing and transporting electrolyte ions. The optimal ZnPC-950 electrode delivers a specific capacitance of 80 $F·g^{-1}$ at 1 $A·g^{-1}$ and cycling durability of 90.9% after 50000 cycles at 10 $A·g^{-1}$. Remarkably, the assembled ZnPC-950// ZnPC-950 symmetric supercapacitor delivers a high energy density of 49.7 $W·h·kg^{-1}$ at a power density of 2477.8 $W·kg^{-1}$, and outstanding electrochemical stability of 85.7% after 10000 cycles in an Et_4NBF_4 electrolyte. This result is superior to most previously reported porous carbon-based supercapacitors in an ionic liquid electrolyte, demonstrating that the aforementioned ZnPCs hold great promise for applications in supercapacitors.

References

1. Poonam S K, Arora A, Tripathi S K. Review of supercapacitors: materials and devices. Journal of Energy Storage, 2019, 21: 801–825

2. Qin Y, Liao Y, Liu J, Tian C, Xu H, Wu Y. Research progress of wood-derived energy storage materials. Journal of Forestry Engineering, 2021, 6(5): 1–13 (in Chinese)

3. Jin Z, Yang L, Shi S, Wang T, Duan G, Liu X, Li Y. Flexible polydopamine bioelectronics. Advanced Functional Materials, 2021, 31(30): 2103391

4. Chen Y, Zhang Q, Chi M, Guo C, Wang S, Min D. Preparation and performance of different carbonized wood electrodes. Journal of Forestry Engineering, 2022, 7(3): 127–135 (in Chinese)

5. Yu J, Liu S, Duan G, Fang H, Hou H. Dense and thin coating of gel polymer electrolyte on sulfur cathode toward high performance Li−sulfur battery. Composites Communications, 2020, 19: 239–245

6. Gonzalez A, Goikolea E, Barrena J A, Mysyk R. Review on supercapacitors: technologies and materials. Renewable & Sustainable Energy Reviews, 2016, 58: 1189–1206

7. Wang G P, Zhang L, Zhang J J. A review of electrode materials for electrochemical supercapacitors. Chemical Society Reviews, 2012, 41(2): 797–828

8. Guo W, Guo X, Yang L, Wang T, Zhang M, Duan G, Liu X, Li Y. Synthetic melanin facilitates MnO supercapacitors with high specific capacitance and wide operation potential window. Polymer, 2021, 235: 124276

9. Han Z, Zhong W, Wang K. Preparation and examination of nitrogen-doped bamboo porous carbon for supercapacitor materials. Journal of Forestry Engineering, 2020, 5(5): 76–83 (in Chinese)

10. Wang Y, Zhang L, Hou H, Xu W, Duan G, He S, Liu K, Jiang S. Recent progress in carbon-based materials for supercapacitor electrodes: a review. Journal of Materials Science, 2021, 56(1): 173–200

11. Yang L, Guo X, Jin Z, Guo W, Duan G, Liu X, Li Y. Emergence of melanin-inspired supercapacitors. Nano Today, 2021, 37: 101075

12. Han X, Xiao G, Wang Y, Chen X, Duan G, Wu Y, Gong X, Wang H. Design and fabrication of conductive polymer hydrogels and their applications in flexible supercapacitors. Journal of Materials Chemistry A: Materials for Energy and Sustainability, 2020, 8(44): 23059–23095

13. You B, Wang L L, Yao L, Yang J. Three dimensional N-doped graphene-CNT networks for supercapacitor. Chemical Communications, 2013, 49(44): 5016–5018

14. Wang W, Lv H, Du J, Chen A. Fabrication of N-doped carbon nanobelts from a polypyrrole tube by confined pyrolysis for supercapacitors. Frontiers of Chemical Science and Engineering, 2021, 15(5): 1312–1321

15. Cheng Y L, Huang L, Xiao X, Yao B, Yuan L Y, Li T Q, Hu Z M, Wang B, Wan J, Zhou J. Flexible and cross-linked N-doped carbon nanofiber network for high performance freestanding supercapacitor electrode. Nano Energy, 2015, 15: 66–74

16. Faraji S, Ani F N. The development supercapacitor from activated carbon by electroless plating—a review. Renewable & Sustainable Energy Reviews, 2015, 42: 823–834

17. Wang N, Huang X, Zhang L, Hu J, Chao Y, Zhao R. Pyrolysis transformation of ZIF-8 wrapped with polytriazine to nitrogen enriched core−shell polyhedrons carbon for supercapacitor. Frontiers of Chemical Science and Engineering, 2021, 15(4):

944–953

18. Hao P, Zhao Z H, Tian J, Li H D, Sang Y H, Yu G W, Cai H Q, Liu H, Wong C P, Umar A. Hierarchical porous carbon aerogel derived from bagasse for high performance supercapacitor electrode. Nanoscale, 2014, 6(20): 12120–12129

19. Wang H, Niu H T, Wang H J, Wang W Y, Jin X, Wang H X, Zhou H, Lin T. Micro-meso porous structured carbon nanofibers with ultra-high surface area and large supercapacitor electrode capacitance. Journal of Power Sources, 2021, 482: 228986

20. Song M Y, Zhou Y H, Ren X, Wan J F, Du Y Y, Wu G, Ma F W. Biowaste-based porous carbon for supercapacitor: the influence of preparation processes on structure and performance. Journal of Colloid and Interface Science, 2019, 535: 276–286

21. Ai T, Wang Z, Zhang H R, Hong F H, Yan X, Su X H. Novel synthesis of nitrogen-containing bio-phenol resin and its molten salt activation of porous carbon for supercapacitor electrode. Materials, 2019, 12(12): 1986

22. Dai J D, Wang L L, Xie A, He J S, Yan Y S. Reactive template and confined self-activation strategy: three-dimensional interconnected hierarchically porous N/O-doped carbon foam for enhanced supercapacitors. ACS Sustainable Chemistry & Engineering, 2020, 8(2): 739–748

23. Dat N T, Tran T T V, Van C N, Vo D V N, Kongparakul S, Zhang H B, Guan G Q, Samart C. Carbon sequestration through hydrothermal carbonization of expired fresh milk and its application in supercapacitor. Biomass and Bioenergy, 2020, 143: 105836

24. Dong D, Zhang Y S, Wang T, Wang J W, Romero C E, Pan W P. Enhancing the pore wettability of coal-based porous carbon as electrode materials for high performance supercapacitors. Materials Chemistry and Physics, 2020, 252: 123381

25. Dong D, Zhang Y S, Xiao Y, Wang T, Wang J W, Gao W. Oxygen-enriched coal-based porous carbon under plasma-assisted $MgCO_3$ activation as supercapacitor electrodes. Fuel, 2022, 309: 122168

26. Chen J, Xiao G, Duan G, Wu Y, Zhao X, Gong X. Structural design of carbon dots/porous materials composites and their applications. Chemical Engineering Journal, 2021, 421: 127743

27. Kong D B, Qin C Y, Cao L, Fang Z M, Lai F L, Lin Z D, Zhang P, Li W, Lin H J. Synthesis of biomass-based porous carbon nanofibre/polyaniline composites for supercapacitor electrode materials. International Journal of Electrochemical Science, 2020, 15(1): 265–279

28. Liu N. Influence of $ZnCl_2$ activation on structure and electrochemical performance of carbon aerogel spheres. Acta Physico-Chimica Sinica, 2013, 29(3): 551–556 (in Chinese)

29. Zhang Q, Yan B, Feng L, Zheng J, You B, Chen J, Zhao X, Zhang C, Jiang S, He S. Progress in the use of organic potassium salts for the synthesis of porous carbon nanomaterials: microstructure engineering for advanced supercapacitors. Nanoscale, 2022, 14(23): 8216–8244

30. Lee K S, Seo Y J, Jeong H T. Capacitive behavior of functionalized activated carbon-based all-solid-state supercapacitor. Carbon Letters, 2021, 31(5): 1041–1049

31. Peng C, Zeng T Q, Kuai Z Y, Li Z F, Yu Y, Zuo J T, Jin Y, Wang Y H, Li L. A self-activation green strategy to fabricate N/P Co-doped carbon for excellent electrochemical performance. Journal of the Electrochemical Society, 2019, 166(14): A3287–A3293

32. Rufford T E, Hulicova-Jurcakova D, Khosla K, Zhu Z H, Lu G Q. Microstructure and electrochemical double-layer capacitance of carbon electrodes prepared by zinc chloride activation of sugar cane bagasse. Journal of Power Sources, 2010, 195(3): 912–918

33. Sandhiya M, Nadira M P, Sathish M. Fabrication of flexible supercapacitor using N-doped porous activated carbon derived from poultry waste. Energy & Fuels, 2021, 35(18): 15094–15100

34. Wu X, Ding B, Zhang C, Li B, Fan Z. Self-activation of nitrogen and sulfur dual-doping hierarchical porous carbons for asymmetric supercapacitors with high energy densities. Carbon, 2019, 153: 225–233

35. Yan D, Liu L, Wang X Y, Xu K, Zhong J H. Biomass-derived activated carbon nanoarchitectonics with hibiscus flowers for high-performance supercapacitor electrode applications. Chemical Engineering & Technology, 2022, 45(4): 649–657

36. Yang B B, Zhang D Y, He J J, Wang Y L, Wang K J, Li H X, Wang Y, Miao L, Ren R Y, Xie M. Simple and green fabrication of a biomass-derived N and O self-doped hierarchical porous carbon via a self-activation route for supercapacitor application. Carbon Letters, 2020, 30(6): 709–719

37. Wang T, Tan S, Liang C. Preparation and characterization of activated carbon from wood via microwave-induced $ZnCl_2$ activation. Carbon, 2009, 47(7): 1880–1883

38. Yue Z, Mangun C L, Economy J. Preparation of fibrous porous materials by chemical activation: 1. $ZnCl_2$ activation of polymer-coated fibers. Carbon, 2002, 40(8): 1181–1191

39. Yao L, Wu Q, Zhang P, Zhang J, Wang D, Li Y, Ren X, Mi H, Deng L, Zheng Z. Scalable 2D hierarchical porous carbon nanosheets for flexible supercapacitors with ultrahigh energy density. Advanced Materials, 2018, 30(11): 1706054

40. Shang Z, An X, Zhang H, Shen M, Baker F, Liu Y, Liu L, Yang J, Cao H, Xu Q, Liu H, Ni Y. Houttuynia-derived nitrogen-doped hierarchically porous carbon for high-performance supercapacitor. Carbon, 2020, 161: 62–70

41. Wang H, Xu Z, Kohandehghan A, Li Z, Cui K, Tan X, Stephenson T J, King'ondu C K, Holt C M B, Olsen B C, Tak J K, Harfield D, Anyia A O, Mitlin D. Interconnected carbon nanosheets derived from hemp for ultrafast supercapacitors with high energy. ACS Nano, 2013, 7(6): 5131–5141

42. Zheng W, Halim J, Persson P O Å, Rosen J, Barsoum M W. MXene-based symmetric supercapacitors with high voltage and high energy density. Materials Reports: Energy, 2022, 2(1): 100078

43. Shao R, Niu J, Liang J, Liu M, Zhang Z, Dou M, Huang Y, Wang F. Mesopore- and macropore-dominant nitrogen-doped hierarchically porous carbons for high-energy and ultrafast supercapacitors in non-aqueous electrolytes. ACS Applied Materials & Interfaces, 2017, 9(49): 42797–42805

44. Wong S I, Lin H, Ma T, Sunarso J, Wong B T, Jia B. Binary ionic liquid electrolyte design for ultrahigh-energy density graphene-based supercapacitors. Materials Reports: Energy, 2022, 2(2): 100093